

Article

Three-Dimensional Modeling of the Thermal Behavior of a Lithium-Ion Battery Module for Hybrid Electric Vehicle Applications

Jaeshin Yi, Boram Koo and Chee Burm Shin *

Department of Energy Systems Research, Ajou University, Suwon 443-749, Korea;
E-Mails: regret@ajou.ac.kr (J.Y.); etaranger@ajou.ac.kr (B.K.)

* Author to whom correspondence should be addressed; E-Mail: cbshin@ajou.ac.kr;
Tel.: +82-31-219-2388; Fax: +82-31-219-1612.

External Editor: Sheng Zhang

Received: 29 August 2014; in revised form: 6 November 2014 / Accepted: 11 November 2014 /
Published: 18 November 2014

Abstract: This paper reports a modeling methodology to predict the effects of operating conditions on the thermal behavior of a lithium-ion battery (LIB) module. The potential and current density distributions on the electrodes of an LIB cell are predicted as a function of discharge time based on the principle of charge conservation. By using the modeling results of the potential and current density distributions of the LIB cell, the non-uniform distribution of the heat generation rate in a single LIB cell within the module is calculated. Based on the heat generation rate in the single LIB cell determined as a function of the position on the electrode and time, a three-dimensional thermal modeling of an LIB module is performed to calculate the three-dimensional velocity, pressure, and temperature distributions within the LIB module as a function of time at various operating conditions. Thermal modeling of an LIB module is validated by the comparison between the experimental measurements and the modeling results. The effect of the cooling condition of the LIB module on the temperature rise of the LIB cells within the module and the uniformity of the distribution of the cell temperatures are analyzed quantitatively based on the modeling results.

Keywords: lithium-ion battery; battery module; thermal model; thermal management

1. Introduction

The lithium-ion battery (LIB) is a preferred power source for hybrid electric vehicle (HEV) applications, because it has a relatively higher energy density, longer cycle life, and lower self-discharge rate as compared to other cell chemistries. As battery temperature greatly affects the performance, safety and life of the LIB for HEV applications, automakers and battery suppliers are paying increased attention to the thermal management for an LIB module [1,2]. In a battery module for HEV applications, depending on the driving conditions and the type of heating and cooling, an uneven temperature distribution can be created in the module. An uneven temperature distribution in an LIB module could lead to an electrical imbalance in the battery module and thus lead to lower performance and shorter battery life. It is, therefore, important to calculate accurately the uneven temperature distribution in a battery module based on modeling to achieve the optimum performance of the battery module [3].

There have been many previous works on the modeling of LIBs and the reviews of LIB models are given in [4,5]. Doyle *et al.* [6] developed a porous electrode model of the lithium polymer battery based on the concentrated solution theory. Others [7–10] used or modified the model of Doyle *et al.* [6]. Kwon *et al.* [11] presented a different approach from the rigorous porous electrode model [6–14] to predict the discharge behavior of an LIB cell. They developed a two-dimensional model to calculate the potential and current density distribution on the electrodes of an LIB cell during constant current discharge by solving the equations derived from the principle of charge conservation. Although they did not include the potential distribution in the electrolyte phase and the lithium ion transport in their model, the model maintains the validity even at high discharge rates and it saves significant computational time as compared to the rigorous porous electrode model. Kim *et al.* [12–14] carried out two-dimensional thermal modeling to predict the thermal behaviors of an LIB cell during discharge and charge on the basis of the potential and current density distributions obtained by following the same procedure of Kwon *et al.* [11]. They resolved two-dimensionally the heat generation rate as a function of position on the electrode of battery cell and state of charge. They found that the distributions of the heat generation rate become more non-uniform as the discharge/charge currents increase under constant-current discharge/charge mode. They reported good agreement between the modeling results and experimental IR (Infrared) measurements. Kim *et al.* [15] and Yi *et al.* [16] extended their thermal model [12,13] to accommodate the dependence of the discharge behavior on the environmental temperature.

Even though Kim *et al.* [12–14] reported the non-uniform distribution of the heat generation rate in an LIB cell during charge and discharge, the heat generation rate in the battery cell was assumed to be uniformly distributed in the many papers related to the thermal modeling for an LIB module or pack published until recently [17–22]. In this work, a three-dimensional modeling is carried out to investigate the effects of operating conditions on the thermal behavior of an LIB module. The non-uniform distribution of the heat generation rate in an LIB cell within the module composed of eight LIB cells is calculated by following the modeling approach for a single LIB cell adopted by Kim *et al.* [12–15]. Thermal modeling of an LIB module is validated by the comparison between the experimental measurements and modeling results.

2. Mathematical Model

The battery module consisting of eight prismatic pouch-type LIB cells fabricated by Top Battery Co. (Ichon, Korea) is modeled in this work. The LIB cell has a nominal capacity of 30 Ah and is composed of lithium nickel manganese cobalt oxide (NMC) positive electrodes, graphite negative electrodes, and porous separators impregnated with plasticized electrolyte. In the battery module, two cells are connected in parallel, composing a single strand, and then four strands are connected in series (2P 4S configuration).

The modeling procedure of a single LIB cell adopted in this work is similar to that of the two-dimensional model of Kwon *et al.* [11]. From the continuity of the current on the electrodes during discharge, the following Poisson equations for the potentials in the positive and negative electrodes can be derived:

$$\nabla^2 V_p = -r_p J \quad \text{in } \Omega_p \quad (1)$$

$$\nabla^2 V_n = +r_n J \quad \text{in } \Omega_n \quad (2)$$

where V_p and V_n are the potentials (V) of the positive and negative electrodes, respectively, r_p and r_n are the resistances (Ω) of the positive and negative electrodes, respectively, and J is the current density (current per unit area (A m^{-2})) transferred through the separator from the negative electrode to the positive electrode. Ω_p and Ω_n denote the computational domains of the positive and negative electrodes, respectively. The resistances, r_p and r_n , are calculated as described in references [11–13]. The relevant boundary conditions for V_p are:

$$\frac{\partial V_p}{\partial n} = 0 \quad \text{on } \Gamma_{p_1} \quad (3)$$

$$V_n = 0 \quad \text{on } \Gamma_{p_2} \quad (4)$$

where $\partial/\partial n$ denotes the gradient in the direction of the outward normal to the boundary. The first boundary condition (3) implies that there is no current flow through the boundary (Γ_{p_1}) of the electrode other than the tab. The second boundary condition (4) means that the linear current density through the tab (Γ_{p_2}) of length L (cm) has a value of I/L . I is the current (A) during discharge. The boundary conditions for V_n are:

$$\frac{\partial V_n}{\partial n} = 0 \quad \text{on } \Gamma_{n_1} \quad (5)$$

$$\frac{1}{r_p} \frac{\partial V_p}{\partial n} = \frac{I}{L} \quad \text{on } \Gamma_{p_2} \quad (6)$$

The first boundary condition (5) implies the same as in the case of V_p . The second boundary condition (6) means that the potential at the tab of the negative electrode has a fixed value of zero as the reference potential. The solutions to Equations (1) and (2) subject to the associated boundary conditions of Equations (3)–(6) are obtained by using a finite element method. The current density (J) of Equations (1) and (2) depends on the polarization characteristics of the electrodes. In this work, the following polarization expression used by Tiedemann and Newman [23,24] is adopted:

$$J = Y(V_p - V_n - U) \quad (7)$$

where Y and U are the fitting parameters. As suggested by Gu [25], U and Y are expressed as functions of the depth of discharge (DOD) as follows:

$$U = a_0 + a_1(\text{DOD}) + a_2(\text{DOD})^2 + a_3(\text{DOD})^3 + \frac{1}{2} \quad (8)$$

$$Y = a_4 + a_5(\text{DOD}) + a_6(\text{DOD})^2 + a_7(\text{DOD})^3 + a_8(\text{DOD})^4 + a_9(\text{DOD})^5 \quad (9)$$

where a_0 – a_9 are the constants that provide the best fit of the modeling results to the experimental data at an environmental temperature. The values of the parameters a_0 – a_9 used in Equations (8) and (9) are given in Table 1. By solving the equations listed above, the distribution of the current density, J , on the electrodes can be obtained as a function of the position on the electrode and time. Therefore, the DOD varies along with the position on the electrode and time elapsed during discharge. The distribution of DOD on the electrode during discharge can be calculated from the distribution of J as follows:

$$\text{DOD} = \text{DOD}_0 + \frac{\int_0^t J dt}{Q_T} \quad (10)$$

where DOD_0 is the initial value of DOD when the discharge process begins, t is the discharge time (s), and Q_T is the theoretical capacity per unit area (Ah m^{-2}) of the electrodes.

After the distributions of the potential and current density on the electrodes of the battery cell are obtained, the heat generation rate within the cell, q , can be calculated as a function of the position on the electrode and time as follows:

$$q = a J \left[V_{oc} - V_{cell} - T \frac{dV_{oc}}{dT} \right] + a_p \frac{|\nabla V_p|^2}{r_p} + a_n \frac{|\nabla V_n|^2}{r_n} \quad (11)$$

where a is the specific area of the battery (m^{-1}), J is the current density (A m^{-2}) calculated by Equation (7), V_{oc} is the open-circuit potential of the cell (V), V_{cell} is the cell voltage (V) obtained through the solutions of Equations (1) and (2), a_p and a_n are the specific area of the positive and negative electrodes (m^{-1}), respectively, and $|\nabla V_p|$ and $|\nabla V_n|$ are the magnitudes of the gradient vectors of ∇V_p and ∇V_n obtained by Equations (1) and (2) (A m^{-1}), respectively. The detailed definition of each term on the right-hand side of Equation (11) is described in references [12,13].

Once the heat generation rate within the single LIB cell is determined as a function of the position on the electrode and time, the information on the heat generation rate of the cell is transferred to the computational fluid dynamics software to perform the three-dimensional thermal modeling of an LIB module. The three-dimensional velocity, pressure, and temperature distributions within the LIB module were calculated as a function of time at various operating conditions by using the computational fluid dynamics (CFD) software ANSYS Fluent 14. A two equations high-Reynolds number turbulence model (k - ϵ) was utilized. Mass flow inlet and pressure outlet boundary conditions are used for the CFD calculations. The inlet boundary conditions for the flow field are set to 0.005781, 0.01156, 0.01734, and 0.02312 kg s^{-1} for the volumetric flow rates of 10, 20, 30, and 40 $\text{ft}^3 \text{min}^{-1}$,

respectively. The outlet boundary condition for the flow field is fixed at 1 atm. The inlet and outlet boundary conditions for the temperature field are the fixed air temperature of 25 °C and the free boundary condition, respectively. The natural-convection boundary condition is used for the outside wall of the module in contact with the environmental air and the value of the heat transfer coefficient used for calculation is $8 \text{ W m}^{-2} \cdot \text{°C}^{-1}$. The finite volume mesh used for calculation has 3,286,950 cells and 693,921 nodes.

Table 1. Values of the fitting parameters a_0 – a_9 used for calculations.

Parameter	Value
a_0 (V)	4.167
a_1 (V)	−1.283
a_2 (V)	1.579
a_3 (V)	−1.115
a_4 (Am^{-2})	47.042
a_5 (Am^{-2})	−179.25
a_6 (Am^{-2})	839.61
a_7 (Am^{-2})	−1759.67
a_8 (Am^{-2})	1713.13
a_9 (Am^{-2})	−635.27

3. Results and Discussion

In order to test the validity of the modeling, the calculated discharge curves based on modeling for the 30 Ah battery fabricated by Top Battery Co. are compared with the experimental data on Figure 1. The experiments were performed at room temperature. At various discharge rates from 1 to 3 C, the experimental discharge curves are in good agreement with the modeling results. After obtaining the distributions of the potential and current density on the electrodes during discharge, the temperature distributions of the battery can be calculated as a function of time for various discharge rates by using the heat generation rate calculated with Equation (11). The temperature distributions based on the experimental IR image and the modeling at the discharge times of 450, 900, and 1800 s with 2 C rate and at the discharge times of 300, 600, and 1200 s with 3 C rate are shown in Figure 2a–c, and Figure 3a–c, respectively. The overall appearances of the temperature distributions from the experiment and modeling are in good agreement. It is observed that the temperature near the current collecting tab of the positive electrode is higher than that of the negative electrode. This phenomenon is due to the fact that the electrical conductivity of the active material of the positive electrode is much lower than that of the negative electrode, although both of the current flows near the tabs of the positive and negative electrodes are similarly high as discussed in references [12,13]. The maximum, average, and minimum temperatures from the experimental measurement for the LIB cell for the discharge rates of 2 and 3 C are compared with those predicted by the modeling in Figure 4a,b, respectively. The maximum, average, and minimum temperatures from the experiment and modeling are in good agreement for the whole range of DOD at both of the discharge rates.

Figure 1. Comparison between experimental and modeling discharge curves at discharge rates of 1, 2, and 3 C. Open symbols are experimental data and solid lines are modeling results.

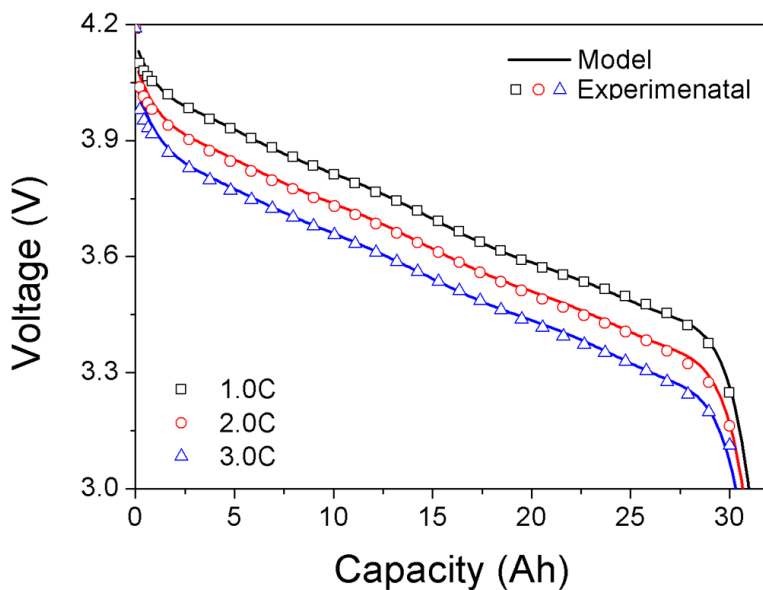


Figure 2. Temperature distributions based on the experimental IR (Infrared) image (upper) and the modeling (lower) for the LIB cell at the discharge times of (a) 450 s, (b) 900 s, and (c) 1800 s with 2 C rate.

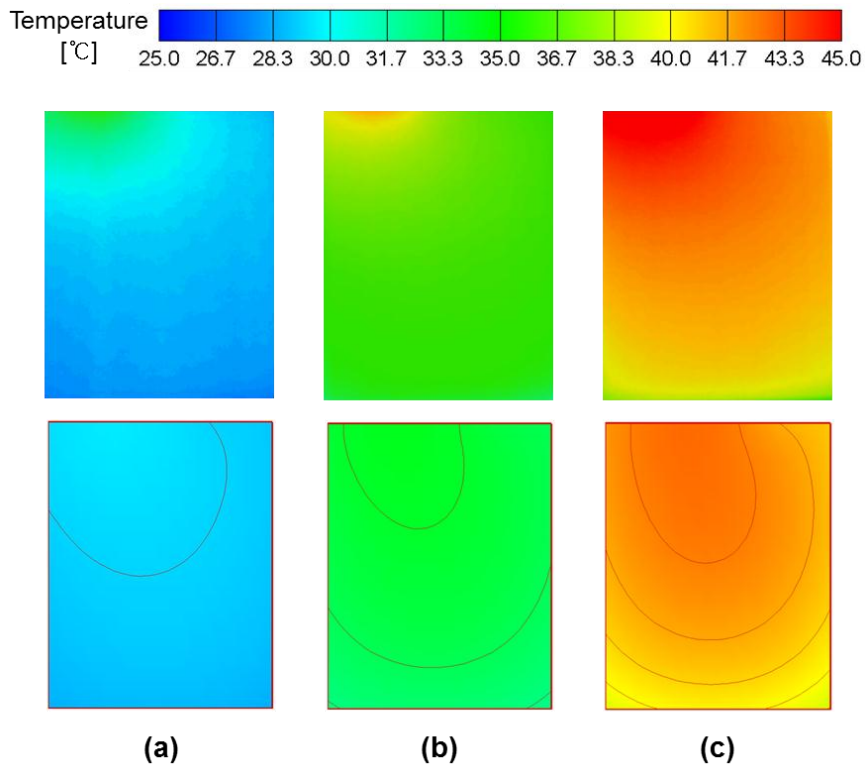


Figure 3. Temperature distributions based on the experimental IR image (**upper**) and the modeling (**lower**) for the LIB cell at the discharge times of (a) 300 s, (b) 600 s, and (c) 1200 s with 3 C rate.

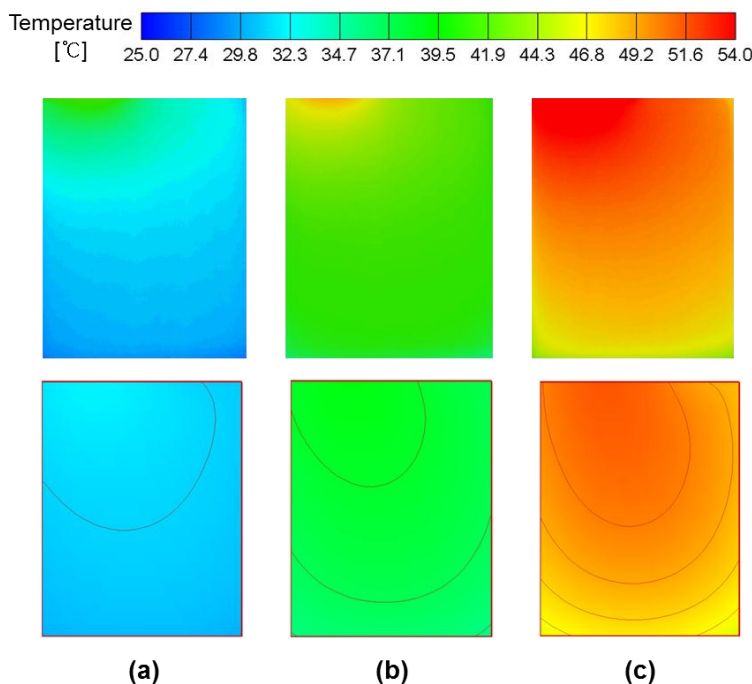
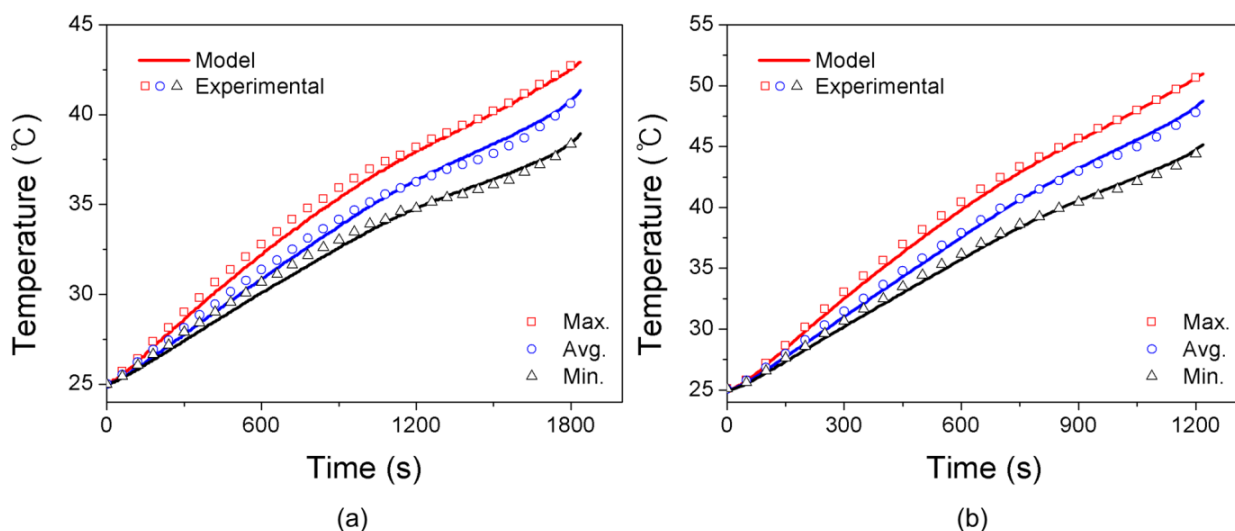


Figure 4. Comparison between the maximum, average, and minimum temperatures from the experiment and modeling at the discharge rates of (a) 2 C and (b) 3 C.



The battery module consisting of 8 prismatic pouch-type LIB cells modeled in this work is shown in Figure 5a. The schematic diagram of the cross section of the module along the line A–A of Figure 5a is given in Figure 5b and the schematic diagram of the cross section along the line B–B of Figure 5a, the direction of cooling air flow, and the positions for thermocouple measurement are shown in Figure 5c.

Figure 5. (a) Photograph of the LIB module; (b) Schematic diagram of the cross section of the module along the line A–A of (a); (c) Schematic diagram of the cross section along the line B–B of (a), the direction of cooling air flow, and the positions for thermocouple measurement; and (d) Finite volume mesh used for CFD (computational fluid dynamics) calculations and the direction of cooling air flow.

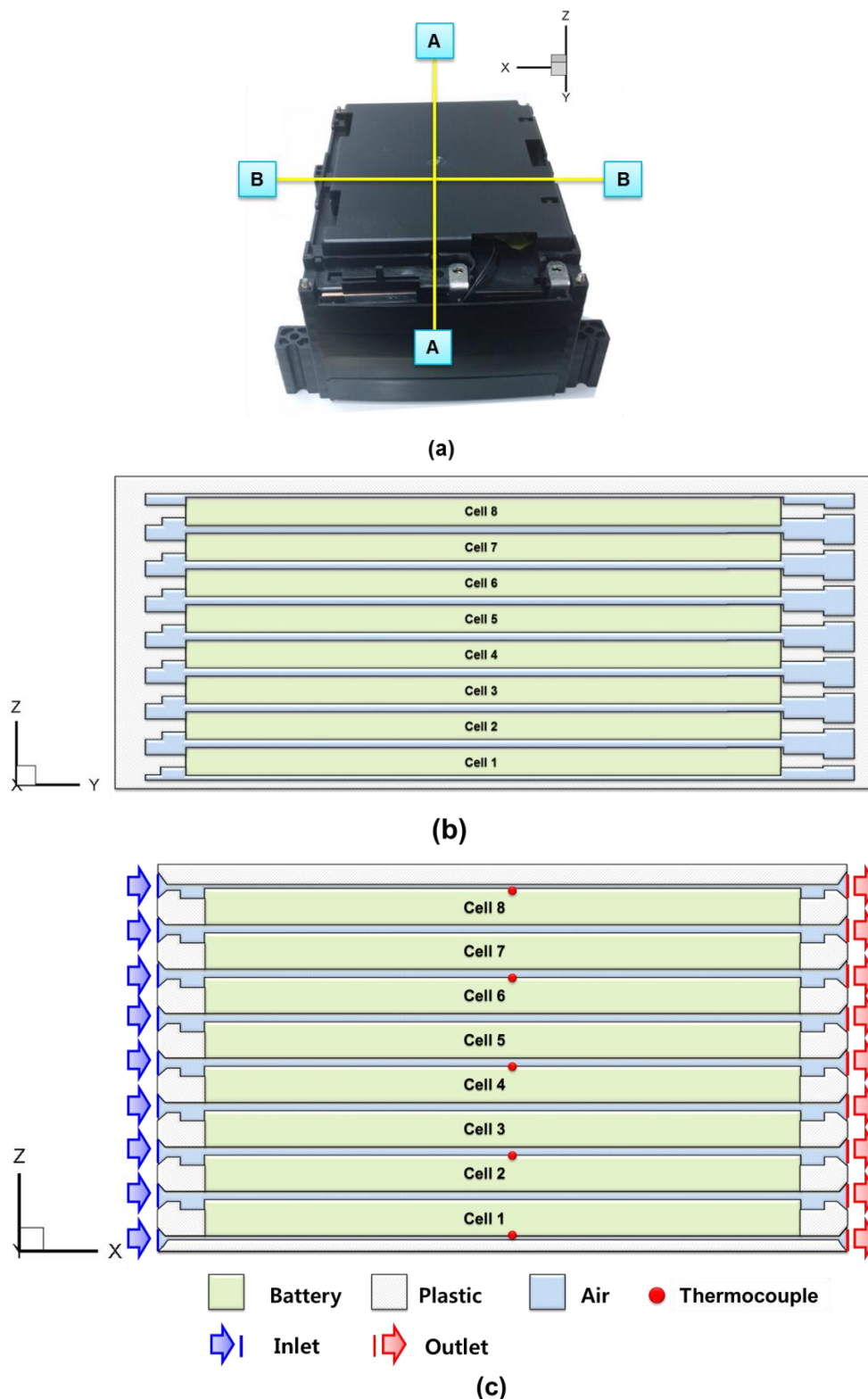
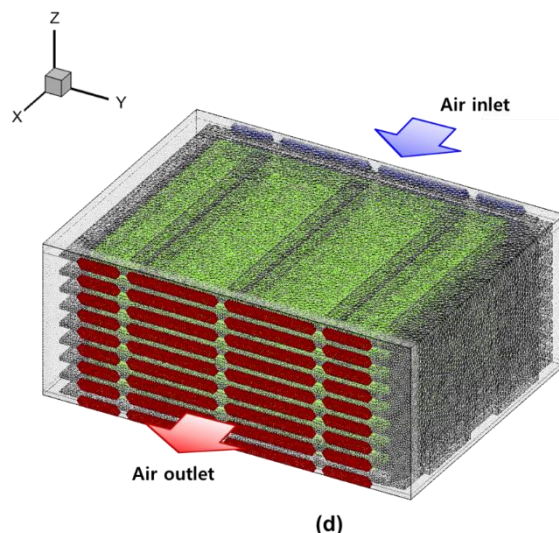


Figure 5. Cont.



The positions for thermocouple measurement are the centers of the rectangular pouch-type cells viewed from the top. Based on the information on the non-uniform distribution of the heat generation rate within the single LIB cell as a function of the position on the electrode and time, the three-dimensional velocity, pressure, and temperature distributions within the LIB module were calculated as a function of time at various operating conditions by using the computational fluid dynamics software ANSYS Fluent 14. The thermal properties of the LIB module compartments used for three-dimensional modeling are given in Table 2.

Table 2. Thermal properties of the LIB module compartments used for three-dimensional modeling.

Thermal Property (unit)	Battery	Aluminum	Air	Plastic
ρ (kg m ⁻³)	2765	2705	1.225	1360
C_p (J kg ⁻¹ · °C ⁻¹)	1394	900	1006	1500
k_x (W m ⁻¹ · °C ⁻¹)	25.7	231	0.0242	0.35
k_y (W m ⁻¹ · °C ⁻¹)	25.7	231	0.0242	0.35
k_z (W m ⁻¹ · °C ⁻¹)	0.794	231	0.0242	0.35

The cell temperatures measured with thermocouple are compared with those calculated from the modeling in Figure 6a,b at various discharge times with the discharge rates of 2 and 3 C, respectively, when the module was cooled in the air by natural convection. Upon the progress of discharge, the cell temperatures increase as shown in Figure 6a,b. Two battery cells located at the bottom and top of the module (#1 and #8) exhibit lower temperature rises than the other cells. The cell temperatures from the modeling agree well with those from the experimental measurement for most of the cells except the cell at the bottom (#1) at the discharge rates of 2 and 3 C. The discrepancy between the cell temperatures from the experiment and modeling for the cell #1, however, increases as the discharge proceeds. This may be due to the fact that the convective boundary condition used for modeling does not reflect the convective heat transfer to which the bottom of the module is exposed in the experiments. In Figures 7 and 8, the temperature distributions of the LIB cells within the module at a few cross sections along the y direction (refer Figure 2a for the y direction) are shown at the discharge

times of 1680 s with 2 C rate and 960 s with 2 C rate, respectively, for natural convection cooling. As shown in Figure 6a,b, the temperatures of the two cells located at the bottom and top of the module are lower than those of the other cells. Along the y direction, the cell temperatures at the cross section close to the left wall of the module shown in Figure 5b are lower than those at the cross section close to the right wall. That seems to be due to the relatively shorter path for heat transfer from the atmospheric air surrounding the module to the cross section close to the left wall as compared to that close to the right wall as can be seen in Figure 5b.

Figure 6. Comparison between the cell temperatures within the module from the experiment and modeling at various discharge times with the discharge rates of (a) 2 C and (b) 3 C for natural convection cooling.

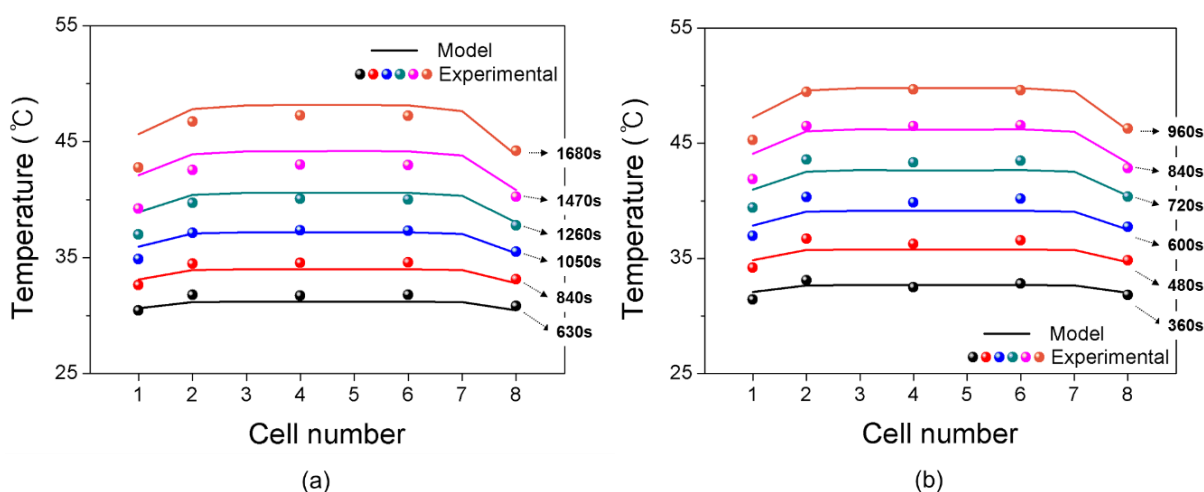


Figure 7. Temperature distributions of the LIB cells within the module at a few cross sections along the y direction at the discharge time of 1680 s with the discharge rate of 2 C for natural convection cooling.

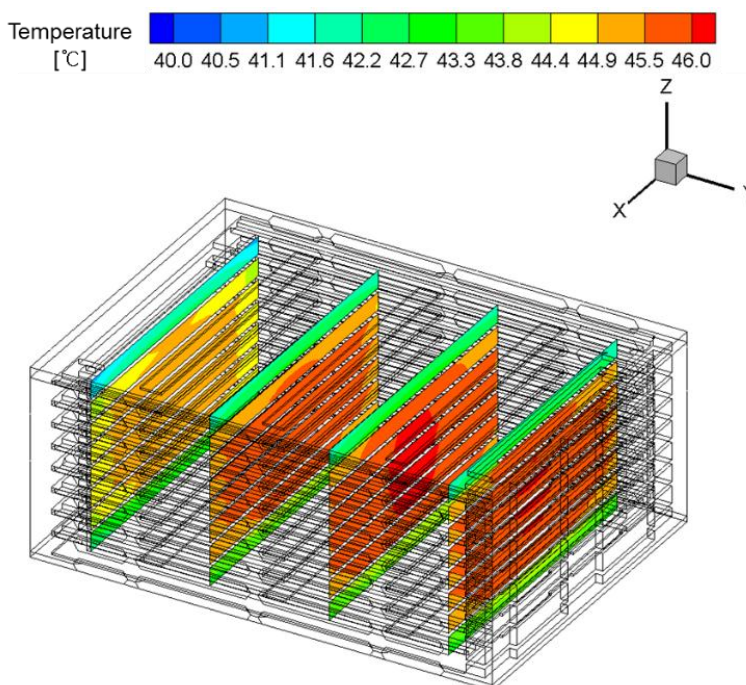
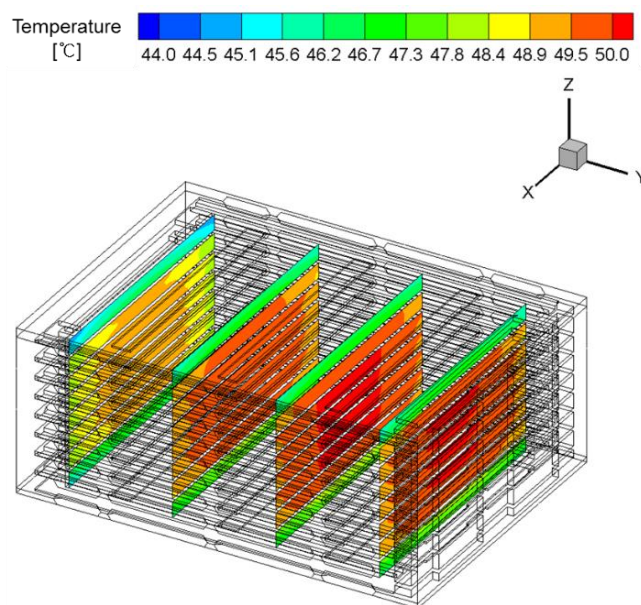


Figure 8. Temperature distributions of the LIB cells within the module at a few cross sections along the y direction at the discharge time of 960 s with the discharge rate of 3 C for natural convection cooling.



In Figure 9a,b, the cell temperatures measured with thermocouple are compared with those calculated from the modeling at different discharge times with the discharge rates of 2 and 3 C, respectively, for various cooling conditions. As compared to the temperature rise for the case of natural convection cooling, it was shown that the temperature rise can be lowered more or less 10 °C near the end of discharge process with the discharge rates of 2 and 3 C by increasing the volumetric flow rate of cooling air up to 40 ft³ min⁻¹, when the module was cooled by forced convection. The temperature rises of the two battery cells located at the bottom and top of the module (#1 and #8) are lower than those of the other cells even for the forced convection cooling. That effect, however, diminishes as the volumetric flow rate of cooling air increases, because the effect of forced convection becomes more dominant at a high volumetric flow rate of cooling air than that of natural convection. The cell temperatures from the modeling agree well with those from the experimental measurement at the discharge rates of 2 and 3 C. The discrepancy between the cell temperatures from the experiment and modeling for the cell #1 that appeared for the natural convection cooling disappears for the forced convection cooling, because the relevance of the convective boundary condition used for modeling at the bottom of the module becomes less important when the effect of forced convection is more dominant at a high volumetric flow rate of cooling air than that of natural convection.

In Figures 10 and 11, the temperature distributions of the LIB cells within the module at a few cross sections along the y direction are shown at the discharge times of 1680 s with 2 C rate and 960 s with 2 C rate, respectively, for various cooling conditions of forced convection. As shown in Figure 9a,b, the temperatures of the two cells located at the bottom and top of the module are lower than those of the other cells, but that effect becomes less significant as the volumetric flow rate of cooling air increases. Along the y direction, the cell temperatures at the cross section close to the left wall of the module are lower than those at the cross section close to the right wall. That effect also becomes less significant as the volumetric flow rate of cooling air increases, because the effect of forced convection

is more dominant at a high volumetric flow rate of cooling air than that of natural convection through the side walls of the module. From the results and discussions on Figures 9–11, we can deduce that the uniformity of the distribution of the cell temperatures within the module increase as the volumetric flow rate of cooling air for forced convection increases. To quantify this effect, the distributions of the volume fraction of the LIB cells within the module as a function of temperature at the discharge times of 1680 s with 2 C rate and 960 s with 2 C rate in Figures 12 and 13, respectively, for various cooling conditions. As shown in Figures 12 and 13, the mean temperatures of the cells within the module decrease and the distributions of the cell temperatures become less dispersed by increasing the volumetric flow rate of cooling air. From the results presented in Figures 12 and 13, we can analyze quantitatively the effect of cooling condition on the temperature rise of the LIB cells within the module and the uniformity of the distribution of the cell temperatures. This analysis is important to the optimal design of the thermal management system for HEV applications, because the LIB temperature and the distribution uniformity of the cell temperature greatly affect the performance, safety and life of the LIB module.

Figure 9. Comparison between the cell temperatures within the module from the experiment and modeling at different discharge times with the discharge rates of (a) 2 C and (b) 3 C for various cooling conditions.

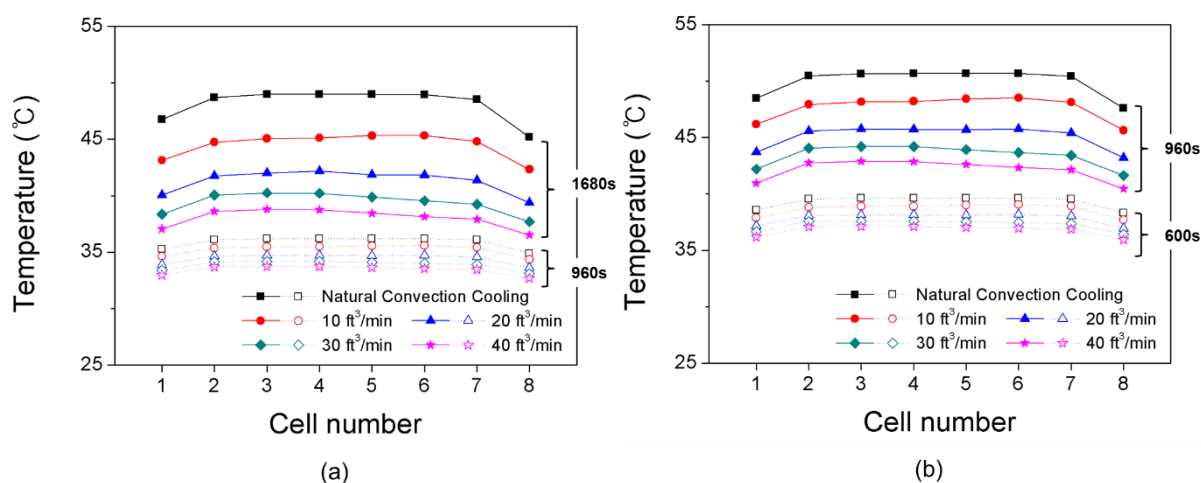


Figure 10. Temperature distributions of the LIB cells within the module at the discharge time of 1680 s with the discharge rate of 2 C for the forced convection cooling with the volumetric flow rates of (a) 10 ft³ min⁻¹, (b) 20 ft³ min⁻¹, (c) 30 ft³ min⁻¹, and (d) 40 ft³ min⁻¹.

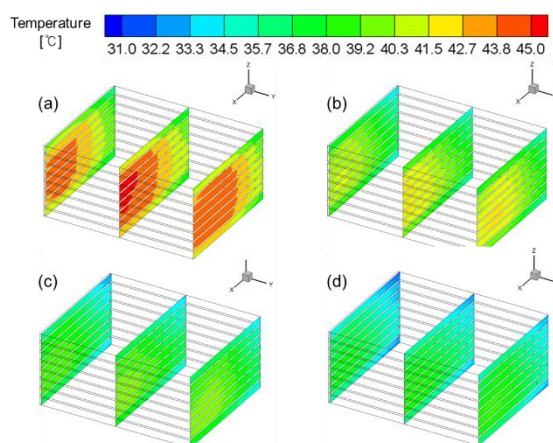


Figure 11. Temperature distributions of the LIB cells within the module at the discharge time of 960 s with the discharge rate of 3 C for the forced convection cooling with the volumetric flow rates of (a) 10 ft³ min⁻¹, (b) 20 ft³ min⁻¹, (c) 30 ft³ min⁻¹, and (d) 40 ft³ min⁻¹.

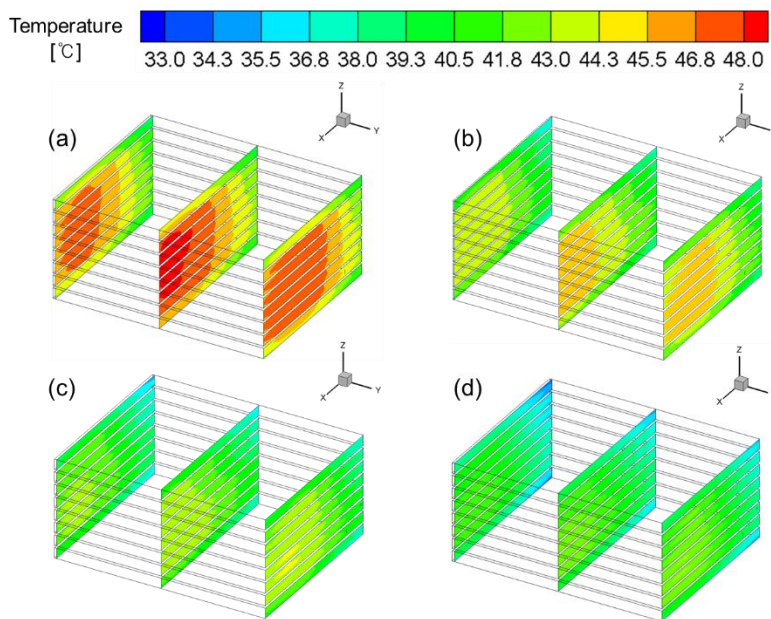


Figure 12. Distributions of the volume fraction of the LIB cells within the module as a function of temperature at the discharge time of 1680 s with the discharge rate of 2 C for various cooling conditions.

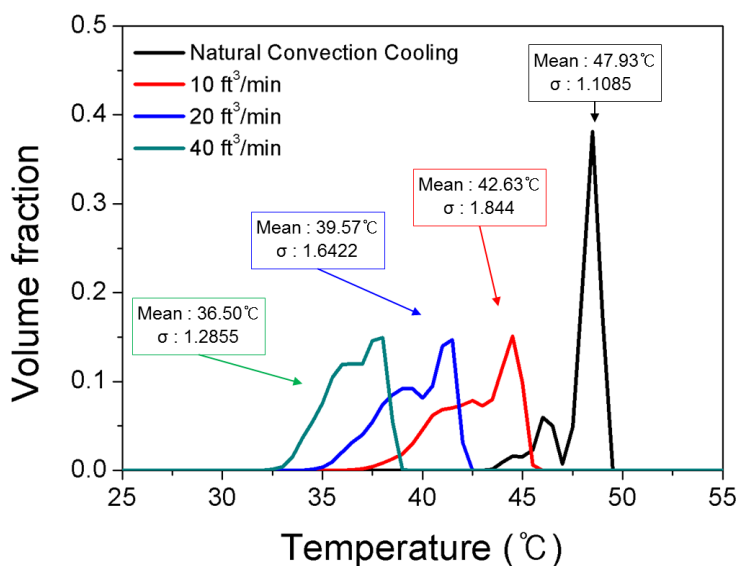
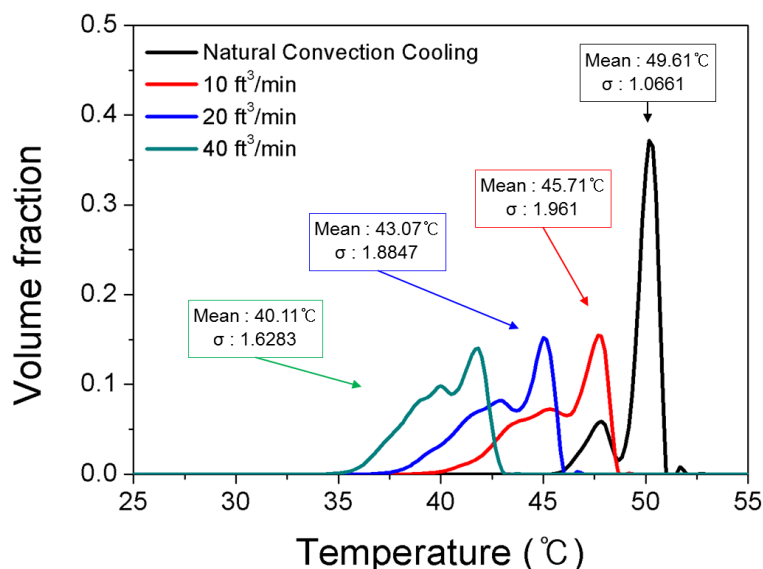


Figure 13. Distributions of the volume fraction of the LIB cells within the module as a function of temperature at the discharge time of 960 s with the discharge rate of 3 C for various cooling conditions.



4. Conclusions

A modeling procedure is developed to study the effects of operating conditions on the thermal behavior of an LIB module. The potential and current density distribution on the electrodes of an LIB cell are predicted as a function of discharge time based on the principle of charge conservation. By using the modeling results of the potential and current density distributions of the LIB cell, the non-uniform distribution of the heat generation rate in a single LIB cell within the module is calculated. The temperature distributions from the modeling of a single LIB cell are in good agreement with those from the experimental IR measurement at the discharge rates of 2 and 3 C. Based on the heat generation rate within the single LIB cell determined as a function of the position on the electrode and time, a three-dimensional thermal modeling of an LIB module is performed to calculate the three-dimensional velocity, pressure, and temperature distributions within the LIB module as a function of time at various operating conditions. Thermal modeling of an LIB module is validated by the comparison between the experimental measurements with thermocouple and the modeling results during discharge with the discharge rates of 2 and 3 C. The thermal modeling results for the case of natural convection cooling of the module are compared to those for the case of forced convection cooling at various volumetric flow rate of cooling air to investigate quantitatively the effect of the cooling condition of the LIB module on the temperature rise of the LIB cells within the module and the uniformity of the distribution of the cell temperatures. The modeling methodology presented in this work may contribute to the optimal design of the thermal management system for HEV applications, because the LIB temperature and the uniformity of the distribution of the cell temperatures within the module are critical to the performance, safety and life of the LIB module.

Acknowledgments

This research was financially supported by the “R&D Infrastructure for Green Electric Vehicle (RE-EV)” through the Ministry of Trade Industry & Energy (MOTIE) and Korea Institute for Advancement of Technology (KIAT).

Author Contributions

Jaeshin Yi prepared a draft of this manuscript, carried out the experimental measurement, and performed the model validation. Boram Koo carried out the modeling and simulation. The whole project was supervised by Chee Burm Shin. All authors revised and approved the manuscript.

Conflicts of Interest

The authors declare no conflict of interest.

References

1. Bandhauer, T.M.; Garimella, S.; Fuller, T.F. A critical review of thermal issues in lithium-ion batteries. *J. Electrochem. Soc.* **2011**, *158*, R1–R25.
2. Williard, N.; He, W.; Hendricks, C.; Pecht, M. Lessons learned from the 787 dreamliner issue on lithium-ion battery reliability. *Energies* **2013**, *6*, 4682–4696.
3. Cedar, G.; Doyle, M.; Arora, P.; Fuentes, Y. Computational modeling and simulation for rechargeable batteries. *MRS Bull.* **2002**, *27*, 619–623.
4. Gomadam, P.M.; Weidner, J.W.; Dougal, R.A.; White, R.E. Mathematical modeling of lithium-ion and nickel battery systems. *J. Power Sources* **2002**, *110*, 267–284.
5. Ramadesigan, V.; Northrop, P.W.C.; De, S.; Santhanagopalan, S.; Braatz, R.D.; Subramanian, V.R. Modeling and simulation of lithium-ion batteries from a systems engineering perspective. *J. Electrochem. Soc.* **2012**, *159*, R31–R45.
6. Doyle, M.; Fuller, T.F.; Newman, J. Modeling of galvanostatic charge and discharge of the lithium/polymer/insertion cell. *J. Electrochem. Soc.* **1993**, *140*, 1526–1533.
7. Gu, W.B.; Wang, C.Y. Thermal-electrochemical modeling of battery systems. *J. Electrochem. Soc.* **2000**, *147*, 2910–2922.
8. Doyle, M.; Fuentes, Y. Computer simulations of a lithium-ion battery and implications for higher capacity next-generation battery designs. *J. Electrochem. Soc.* **2003**, *150*, A706–A713.
9. Srinivasan, V.; Wang, C.Y. Analysis of electrochemical and thermal behavior of Li-ion Cells. *J. Electrochem. Soc.* **2003**, *150*, A98–A106.
10. Ramadass, P.; Haran, B.; Gomadam, P.M.; White, R.E.; Popov, B.N. Development of first principles capacity fade model for Li-ion cells. *J. Electrochem. Soc.* **2004**, *151*, A196–A203.
11. Kwon, K.H.; Shin, C.B.; Kang, T.H.; Kim, C.S. A Two-dimensional modeling of a lithium-polymer battery. *J. Power Sources* **2006**, *163*, 151–157.
12. Kim, U.S.; Shin, C.B.; Kim, C.S. Effect of electrode configuration on the thermal behavior of a lithium-polymer battery. *J. Power Sources* **2008**, *180*, 909–916.

13. Kim, U.S.; Shin, C.B.; Kim, C.S. Modeling for the scale-up of a lithium-ion polymer battery. *J. Power Sources* **2009**, *189*, 841–846.
14. Kim, U.S.; Yi, J.; Shin, C.B.; Han, T.; Park, S. Modeling for the thermal behavior of a lithium-ion battery during charge. *J. Power Sources* **2011**, *196*, 5115–5121.
15. Kim, U.S.; Yi, J.; Shin, C.B.; Han, T.; Park, S. Modeling the dependence of the discharge behavior of a lithium-ion battery on the environmental temperature. *J. Electrochem. Soc.* **2011**, *158*, A611–A618.
16. Yi, J.; Kim, U.S.; Shin, C.B.; Han, T.; Park, S. Modeling the temperature dependence of the discharge behavior of a lithium-ion battery in low environmental temperature. *J. Power Sources* **2013**, *244*, 143–148.
17. Chen, S.C.; Wan, C.C.; Wang, Y.Y. Thermal analysis of lithium-ion batteries. *J. Power Sources* **2005**, *140*, 111–124.
18. Spotnitz, R.M.; Weaver, J.; Yeduvaka, G.; Doughty, D.H.; Roth, E.P. Simulation of abuse tolerance of lithium-ion battery packs. *J. Power Sources* **2013**, *244*, 143–148.
19. Zhu, C.; Li, X.; Song, L.; Xiang, L. Development of a theoretically based thermal model for lithium ion battery pack. *J. Power Sources* **2013**, *223*, 155–164.
20. Xu, X.M.; He, R. Research on the heat dissipation performance of battery pack based on forced air cooling. *J. Power Sources* **2013**, *240*, 33–41.
21. Fathabadi, H. A novel design including cooling media for lithium-ion batteries pack used in hybrid and electric vehicles. *J. Power Sources* **2014**, *245*, 495–500.
22. Sabbah, R.; Kizilel, R.; Selman, J.R.; Al-Hallaj, S. Active (air-cooled) vs. passive (phase change material) thermal management of high power lithium-ion packs: Limitation of temperature rise and uniformity of temperature distribution. *J. Power Sources* **2008**, *182*, 630–638.
23. Tiedemann, W.; Newman, J. Current and potential distribution in lead-acid battery plates. In *Battery Design and Optimization*; Gross, S., Ed.; The Electrochemical Society, Inc.: Pennington, NJ, USA, 1979; pp. 39–49.
24. Newman, J.; Tiedemann, W. Potential and current distribution in electrochemical cells interpretation of the half-cell voltage measurements as a function of reference electrode location. *J. Electrochem. Soc.* **1993**, *140*, 1961–1968.
25. Gu, H. Mathematical analysis of a Zn / NiOOH cell. *J. Electrochem. Soc.* **1983**, *130*, 1459–1464.